RSC Advances

PAPER

View Article Online
View Journal | View Issue

Cite this: *RSC Adv.*, 2025, **15**, 21051

Macroporous C@MoS_2 composite as anodes for high-performance sodium-ion batteries†

Yan Yang, ‡*[a] Lei Wang,‡[ab] Cong Suo[a] and Yining Liu[a]

Received 20th February 2025
Accepted 9th June 2025

DOI: 10.1039/d5ra01240f

rsc.li/rsc-advances

Sodium-ion batteries (SIBs) are considered promising energy storage devices and substitutes for lithium-ion batteries in the near future, and their anode materials play crucial roles in their electrochemical performance. Molybdenum disulfide (MoS_2) has attracted significant attention as an SIB anode material owing to its high theoretical capacity (670 mA h g^{-1}) and 2D structure with a large layer space (0.65 nm *vs.* 0.33 nm of graphite). In this work, 3D polystyrene (PS) microspheres were adopted as sacrificial templates to construct a hierarchical macroporous C@MoS_2 composite, which has rarely been reported for SIB anodes. This unique design synergistically integrated conductive macroporous carbon networks with 2D-layered MoS_2, enabling super Na^+ storage capability and unprecedented cycling stability in SIBs. In particular, a capacity of 438 mA h g^{-1} after 100 cycles at a current density of 500 mA g^{-1} and a capacity of 319.4 mA h g^{-1} after 1000 cycles at 1000 mA g^{-1} were achieved owing to its unique macroporous structure. Furthermore, the high electronic conductivity, large surface area, and rich Na^+ diffusion channels all benefit for its super capacity and stability.

1. Introduction

The intermittent output property of renewable energy has pushed the rapid development of energy storage systems, such as lithium-ion batteries (LIBs),[1,2] super capacitors,[3] redox flow batteries, and sodium-ion batteries (SIBs).[4] Among these, SIBs have shown great industrial application potential owing to their low cost, rich reserves, and similar structures and reaction mechanisms with those of commercial LIBs.[5,6] Meanwhile, compared with LIBs, SIBs have many advantages in terms of low-temperature performance, rate performance, and safety.[6–8] However, there is a big difference between SIBs and LIBs, especially in anode materials.[9–11] Na^+ (0.102 nm) is not thermodynamically stable in graphite because of its weak Na–C interaction.[12–14] Therefore, the development of suitable anode materials is imminent for the rapid development of SIBs.

Molybdenum disulfide (MoS_2) has a typical 2D layered structure, which is similar to graphite but with a larger layer space (0.65 *vs.* 0.33 nm), and it has shown great potential as an anode material in SIBs;[15–17] however, the inherent low conductivity and instability caused by MoS_2's high surface energy hinder its wide application. To address these drawbacks, various strategies have been adopted, such as changing the structure or morphology of MoS_2, expanding the layer spacing of MoS_2, and making carbon-based composites to improve both the conductivity and stability of MoS_2 nanosheets.[16,18–20] Variable carbon–MoS_2 composites with different compositions and structures were reported to show good potential in SIBs;[21–28] for example, Zheng *et al.* prepared 3D MoS_2 with a macroporous foam structure through SiO_2 templates, and this material showed superior specific capacity and cycling stability in SIBs.[29] However, HF or strong alkali was needed to remove SiO_2 templates, which was dangerous and time-consuming. Therefore, it is crucial to develop a more facile and eco-friendly method to build macroporous carbon–MoS_2 composites with high SIB performance.

Herein, a carbon–MoS_2 composite with a macroporous structure was fabricated through a facile hydrothermal method using 3D polystyrene (PS) microspheres as templates. The 3D PS templates could be easily removed during the carbonization process, providing an efficient way to build carbon–MoS_2 composite structures with tuneable macropore sizes. The sample showed an excellent cell capacity of 438 mA h g^{-1} after 100 cycles at a current density of 500 mA g^{-1} and super stability with a capacity of 319.4 mA h g^{-1} after 1000 cycles at 1000 mA g^{-1}. This performance stemmed from (i) hierarchical Na^+ and charge transport pathways through interconnected macroporous carbon networks, (ii) enhanced surface area and reactive sites from well-dispersed MoS_2 nanosheets, and (iii) relieved mechanical stress and volume expansion during cycling from the macroporous network.

[a]*SINOPEC (Dalian) Research Institute of Petroleum and Petrochemicals Co., Ltd, China. E-mail: yangyan.fshy@sinopec.com*

[b]*College of Environmental Science and Engineering, Dalian Maritime University, Dalian 116026, China*

† Electronic supplementary information (ESI) available: The characterization results of PS nanospheres and control sample. See DOI: https://doi.org/10.1039/d5ra01240f

‡ These authors contributed equally to this work.

2. Experimental

2.1 Preparation of 3D PS templates

50 mL of styrene was added to a three-necked round-bottom flask containing 500 mL of water; then, 2.5 g of PVP was added under a N_2 atmosphere. 1 g $K_2S_2O_8$ was dissolved in 50 mL of deionized water and was quickly added to the flask to initiate the polymerization reaction of styrene. After being stirred at 94 °C for 24 h, the mixture was cooled, and monodispersed polystyrene nanospheres in colloidal form were obtained. It is worth noting that the stirring speed during the polymerization process should be kept below 500 rpm. Overnight vacuum filtration of these polystyrene nanospheres yields 3D PS templates.

2.2 Synthesis of porous C@MoS_2

100 mg of 3D PS nanospheres were dissolved in 50 mL of deionized water under ultrasonic treatment. Then, 500 mg of glucose, 300 mg of sodium molybdate, and 600 mg of thiourea were added in turn, and then the mixture was placed into an autoclave for hydrothermal treatment at 200 °C for 24 h. After the autoclave was cooled, the sample was collected and washed using DI water and ethanol to remove organic impurities and surface impurities from the products and then dried in an oven at 80 °C for 24 h. The dried sample was carbonized at 800 °C for 2 h, and the atmosphere used for the carbonization process was N_2 with a flow rate of 50 mL min^{-1} in a tubular furnace, and the porous C@MoS_2 composite sample was obtained. No washing occurred after the carbonization process.

2.3 Synthesis of C@MoS_2 control sample

The synthesis is similar to porous C@MoS_2, but without the addition of PS templates, the other steps are the same.

2.4 Materials characterization

High-resolution scanning electron microscopy (HRSEM) was conducted using Hitachi S5500. High-resolution transmission electron microscopy (HRTEM) was conducted using the TECNAI G2 F30. X-ray diffraction (XRD) measurements were conducted on Rigaku D/Max 2500/PC. Raman spectroscopy was performed using a LabRAM HR 800 Raman spectrometer. XPS was carried out using KRATOS Axis Ultra DLD. The vacuum degree in the analysis room was 9.8×10^{-10} Torr. The TGA was carried out in an air atmosphere using a Netzsch thermogravimetric TG 209 F3 Tarsus® analyzer with a heating rate of 5 °C min^{-1} till 700 °C and then cooled naturally. The nitrogen sorption experiments were performed at 77 K using Micromeritics ASAP 2020. The CO_2 sorption experiments were performed at Micromeritics TriStar II 3020.

2.5 Electrochemical characterization

The battery was assembled using a CR2032 coin cell. By mixing the active material, acetylene black, and polyvinylidene fluoride as a binder at a weight ratio of 7 : 2 : 1; then pasting it onto a Cu foil current collector and drying in a vacuum oven at 60 °C, the anode was made. The acetylene black and binder content in the electrode composition (7 : 2 : 1) enhances mechanical integrity and electronic conductivity, which are crucial for MoS_2 electrodes that have significant volume changes and low inherent conductivity during cycling. Although it may reduce electrode mesoporosity, optimizing this content is necessary to balance structural stability, electronic conductivity and ion transportation rate for better performance. Metallic Na pieces were used as counter/reference electrodes. Although two-electrode cells are simpler and more commonly used, they have the potential drawbacks of reference/counter electrode polarization at high current densities in SIBs; therefore, three-electrode cells are recommended when it is available.[30,31] A glass fiber membrane (Whatman/F) was used as a separator. The electrolyte is formed by 1 M $NaClO_4$ in EC : PC (1 : 1 vol%) + 5 wt% FEC. The galvanostatic discharge/charge measurements were performed in the voltage range of 0.01–3 V (*vs.* Na/Na^+) on a NEWARE battery testing system. Cyclic voltammetry (CV) and electrochemical impedance spectroscopy (EIS) tests were performed at an electrochemical workstation (Autolab). CV was measured in a voltage range of 0.01–3 V at room temperature. The EIS of the electrodes was measured by applying a 5 mV amplitude signal at a frequency of 0.01 Hz to 100 kHz.

3. Results and discussion

PS nanospheres can be used as hard templates to build 2D or 3D macroporous structures because they can be easily removed.[32,33] The preparation process of porous C@MoS_2 is facile, as shown in Fig. 1. Only a one-pot hydrothermal treatment and carbonization process are required. 3D PS nanospheres were prepared by overnight vacuum filtration, and after drying, it was used as a template for the 3D macrospore fabrication of Porous C@MoS_2. As shown in Fig. S1,† the PS nanospheres exhibit a regular spherical shape with a uniform particle size distribution of ~200 nm. After overnight vacuum filtration, the PS nanospheres gather together and form an ordered 3D arrangement, which is an ideal template for preparing macroporous structures. PS templates, glucose, sodium molybdate, and thiourea were mixed and hydrothermally treated at 200 °C for 24 h. Then, 2D layered-MoS_2 and carbon precursors were coated on 3D PS templates. After carbonization at 800 °C for 2 h, the porous C@MoS_2 composite sample was obtained.

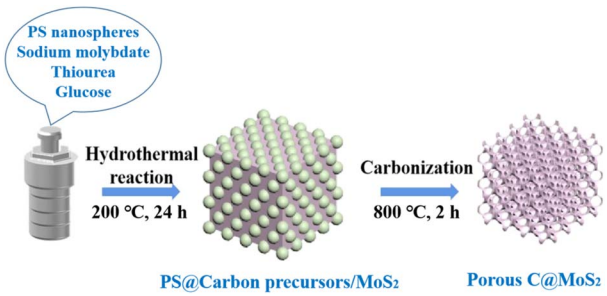

Fig. 1 Schematic of the preparation process of porous C@MoS_2.

The scanning electron microscopy (SEM) image of porous C@MoS_2 is shown in Fig. 2a, demonstrating the nano-sized spherical morphology with a typical 2D-layered structure of MoS_2 on their surface (~350 nm). Transmission electron microscopy (TEM) further confirmed its macroporous structure with a pore size of ~200 nm, which is the same as the diameter of the prepared PS nanospheres. Molybdenum disulfide nanosheets are massively generated on a macroporous carbon framework, providing solid contact with carbon while exhibiting a high surface area of MoS_2. No PS nanospheres were found, indicating the complete removal of PS templates after high-temperature carbonization.[34–39] The high-resolution transmission electron microscopy (HRTEM) image shown in Fig. S2† reveals a layered lattice spacing of 0.77 nm, matching the (002) plane of 2H-MoS_2, confirming the well-preserved layered structure of MoS_2 in porous C@MoS_2. Finally, elemental mapping tests (Fig. 2c–f) show a uniform distribution of Mo, S, and C elements, indicating a uniform distribution of molybdenum disulfide on the macroporous carbon framework.[40]

To illustrate the importance of this novel macroporous structure, a control sample without a pore structure design was fabricated under similar conditions, denoted as C@MoS_2. In Fig. S3,† it is found that only micron-sized carbon particles were obtained, with MoS_2 nanosheets coated on their surfaces.

The XRD results of porous C@MoS_2 and C@MoS_2 depicted in Fig. 3a clearly show the diffraction peaks at 2θ of 33.04°, 39.64° and 58.58°, corresponding to (100), (103) and (110) planes of MoS_2, respectively.[41] The absence of (002) reflections indicates that the MoS_2 mainly exists in single layers or few layers in these C@MoS_2 composites.[42] The 17.8° diffraction peak is likely attributed to the (004) diffraction peak, indicating the presence of the 1T phase of molybdenum disulfide.[43] The XRD patterns were examined using the same XRD machine. The relatively weak peak intensity of C@MoS_2 suggests that the MoS_2 possesses poor crystallinity. Moreover, the absence of the 17.8° diffraction peak in C@MoS_2 may signify that it does not contain or contains only a negligible amount (below the detection threshold of the XRD) of (004) planes, thereby further confirming its poor crystallinity. The characteristic peaks of the in-plane mode of E^1_{2g} at 379.1 cm^{-1} and the out-of-plane mode of A_{1g} at 403.2 cm^{-1} in MoS_2 can be clearly observed in the Raman spectra.[44] The two characteristic peaks at 1357.3 cm^{-1} and 1592.4 cm^{-1} in Fig. 3b correspond to the D (disordered) band and G (graphite) band of the carbon material derived from glucose carbonization, with the D band relatively stronger, indicating the existence of carbon defects in both samples. Based on the Raman analysis, the D/G ratios of porous C@MoS_2 and C@MoS_2 are 2.58 and 1.89, respectively. This suggests that the porous C@MoS_2 material exhibits a higher degree of structural disorder and defects, which can be attributed to its porous structure.[45]

The surface chemistry of porous C@MoS_2 was determined by X-ray photoelectron spectroscopy (XPS). Three peaks centered at 226.5, 229.3 and 232.5 eV are observed in the high-resolution XPS spectrum of Mo 3d (Fig. 4b), which are attributed to S 2s, Mo $3d^{5/2}$ and Mo $3d^{3/2}$, respectively. Meanwhile, the peak at 235.3 eV is assigned to Mo^{6+} $3d^{3/2}$,[46,47] which is formed by the oxidation of Mo^{4+} in air. In the S 2p spectrum of porous C@MoS_2, two peaks are observed at 162.3 and 163.5 eV, which is assigned to S $2p^{3/2}$ and S $2p^{1/2}$,[48,49] respectively (Fig. 4c). A peak was also found at 168.7 eV, which may be caused by the oxidation of the S in the air. Fig. 4d illustrates three peaks at 284.6, 285.74, and 288.7 eV, corresponding to C–C, C–O, and C=O, respectively.[50,51] XPS spectra of C@MoS_2 show similar peaks, confirming the same chemical configuration with porous C@MoS_2, as shown in Fig. S4.†

The MoS_2 content was determined by thermogravimetric analysis (TGA). In Fig. S5,† there are three mass losses in porous C@MoS_2. The first mass loss (<200 °C) was generated by the evaporation of water that the sample adsorbed from the

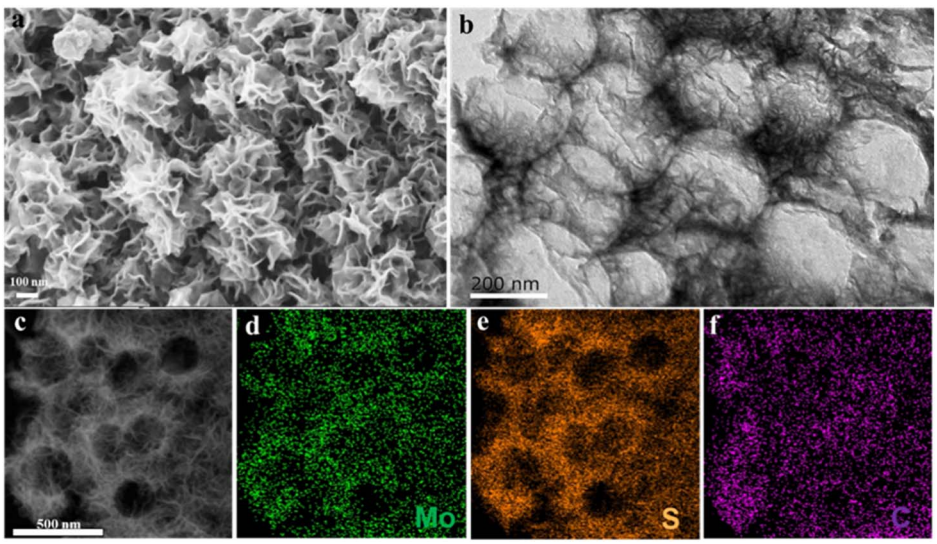

Fig. 2 Morphology and nanostructure characterizations of porous C@MoS_2. SEM image (a), TEM image (b), high angle annular dark field-scanning transmission electron microscopy (HAADF-STEM) image (c), and the corresponding EDS elemental mapping images of Mo (d), S (e) and C (f).

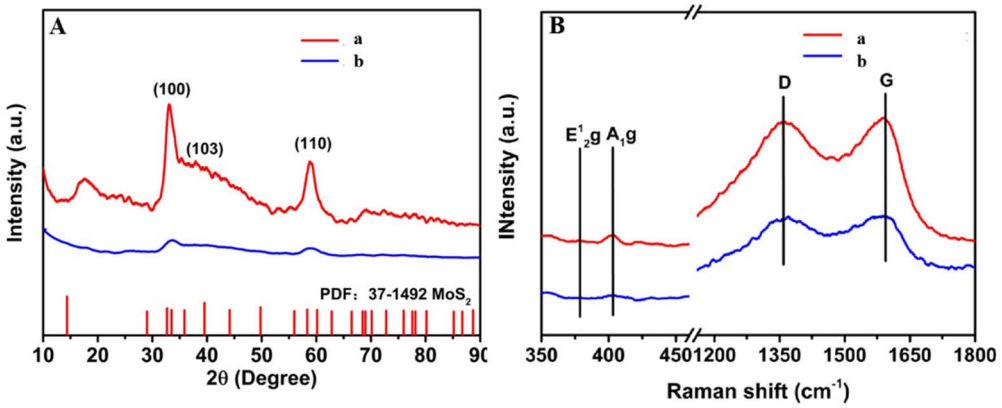

Fig. 3 Structure and composition characterizations of porous C@MoS_2 and C@MoS_2. (A) XRD patterns. (B) Raman spectra.

atmosphere. The second loss in the range of 200–370 °C is attributed to the oxidation of MoS_2 ($2MoS_2 + 7O_2 \rightarrow 2MoO_3 + 4SO_2$), while the third loss from 400 °C to 490 °C is attributed to the combustion of carbon.[52,53] Based on TGA results, assuming the product at 600 °C is pure MoO_3, the MoS_2 contents in porous C@MoS_2 and C@MoS_2 are calculated to be 58.2 wt% and 70.4 wt%, respectively. Compared to C@MoS_2 without templates, porous C@MoS_2 has a lower MoS_2 content probably owing to the use of PS templates altering their ratio based on the adsorption affinity of carbon and MoS_2 precursors to PS

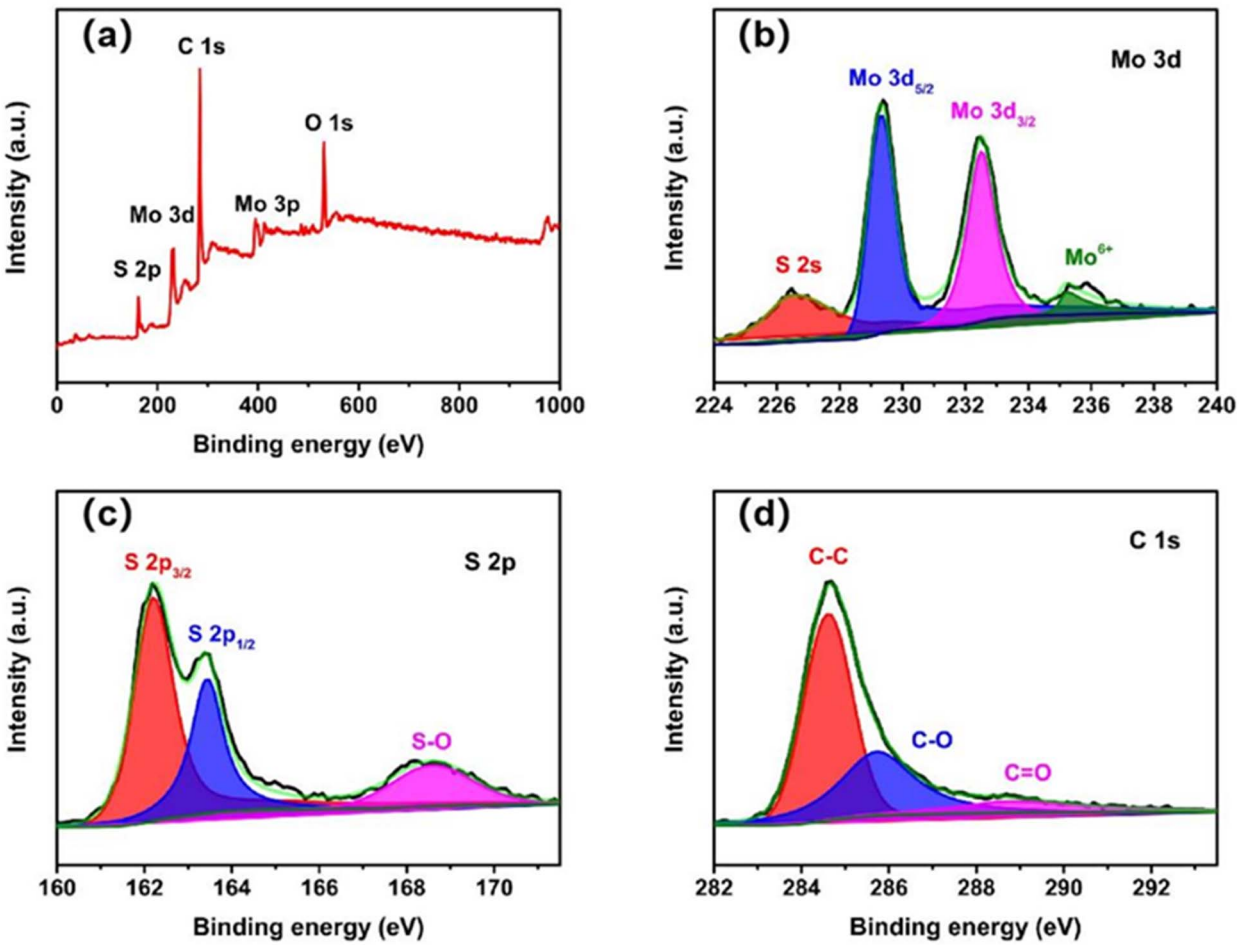

Fig. 4 Composition characterization of porous C@MoS_2. XPS survey spectrum (a) and high-resolution XPS spectra of Mo 3d (b), S 2p (c), and C 1s (d).

spheres. Both N_2 and CO_2 adsorption and desorption isotherms of porous C@MoS_2 and C@MoS_2 were tested to fully reveal their difference in pore structures. Porous C@MoS_2 demonstrates a significantly higher surface area, 58.4 m^2 g^{-1} through N_2 adsorption and 65.8 m^2 g^{-1} *via* CO_2 adsorption, in contrast to C@MoS_2, which exhibits surface areas of 9.1 m^2 g^{-1} by N_2 and 45.2 m^2 g^{-1} by CO_2 (Fig. S6 and S7†).[54] Therefore, using 3D PS nanospheres as templates, we successfully fabricated a novel 3D MoS_2 macroporous material with high MoS_2 loading and surface area.

Fig. 5a shows the first five CV curves of porous C@MoS_2 at scan rates of 0.5 mV s^{-1} in the range of 0.01–3.0 V. In the initial CV cycle of porous C@MoS_2 and C@MoS_2 (Fig. S8†), the reduction peaks observed at ~0.7 V are attributed to the insertion of Na^+ ions between the MoS_2 layers, and the formation of a solid electrolyte interface (SEI) layer, which results from the decomposition of the electrolyte. The reduction peaks at ~0.3 V are associated with the further formation of Mo and Na_2S through the conversion reaction ($Na_xMoS_2 + Na^+ + e^- \rightarrow 2Na_2S$ + Mo) and the insertion of Na^+ ions into the graphitic carbon. The significant oxidation peaks at ~1.75 V correspond to the oxidation conversion reaction of Mo with partial Na_2S to reform MoS_2.[55] The second to fifth discharge/charge curves almost overlap, indicating the high reversibility and cycling stability of Na^+ storage in porous C@MoS_2 composites.[56,57] Compared with C@MoS_2, porous C@MoS_2 possesses a much larger CV area and higher peak currents, indicating its high charge storage capacity and fast kinetics for charging/discharging reactions. The second to fifth discharge/charge curves almost overlap, indicating the high reversibility and cycling stability of Na^+ storage in porous C@MoS_2 composites. As depicted in Fig. 5b, compared to C@MoS_2, the porous C@MoS_2 shows a much higher initial discharge capacity of 1024 mA h g^{-1} (*vs.* 740 mA h g^{-1}, Fig. S9†) at a current density of 0.5 A g^{-1}, and the irreversible capacity loss in the second cycle is mainly caused by the decomposition of electrolyte and the formation of SEI film. The initial coulombic efficiency for Porous C@MoS_2 and C@MoS_2 is 62.46% and 58%, respectively. This is probably because, during the initial charge–discharge cycle, the electrode material may undergo significant changes during SEI formation, preventing some sodium ions from being smoothly extracted from the structure, thereby reducing coulombic efficiency. For the third, tenth, and 100th cycles, the charge/discharge curves were found to almost overlap, with a discharge capacity of 452 mA h g^{-1} after 100 cycles, indicating the good stability of the porous C@MoS_2 sample. Fig. 5c presents the rate performance of the porous C@MoS_2. The discharge capacities of porous C@MoS_2 are 471, 453, 420, 386, 365 and 338 mA h g^{-1} when the current densities are 50, 100, 300, 500, 1000 and 2000 mA g^{-1}, respectively, which are significantly higher than those (375, 348, 325, 300, 286 and 266 mA h g^{-1}, respectively) of the C@MoS_2 sample. Surprisingly, when returning to low current density after high-rate cycling, the capacity can still return to the original level at 0.1 A g^{-1}, which further illustrates the excellent reversibility of the material. Next, we conducted a cycle stability test using porous C@MoS_2 and C@MoS_2 for 100 cycles at 0.5 A g^{-1}. Once again, porous C@MoS_2 showed better performance when compared with the control sample (441 *vs.* 346 mA h g^{-1}), which may be caused by its novel structure, with a macroporous structure providing high surface area and relieving mechanical stress and volume change during charging/discharging processes. In addition, long-term cycling stability tests were conducted at a high current density of 1000 mA g^{-1}. Fig. 5e shows that it still has a capacity of 319.4 mA h g^{-1} after 1000 cycles with a coulombic efficiency of 99.7%. In comparison to porous C@MoS_2, C@MoS_2 exhibited a relatively lower capacity during the long-term cycling tests. It delivered an initial capacity of 358 mA h g^{-1}, which is significantly lower than the 580 mA h g^{-1} of porous C@MoS_2. After 1000 cycles at 1000 mA g^{-1}, C@MoS_2 retained a capacity of 223.1 mA h g^{-1} (Fig. S11†), while porous C@MoS_2 maintained a higher capacity of 319.4 mA h g^{-1}. The enhanced performance of porous C@MoS_2 may be attributed to its unique structure, featuring a macroporous architecture that offers a high surface area and mitigates mechanical stress and volume changes during the charging and discharging cycles.

Electrochemical impedance spectroscopy (EIS) represents the Na^+ diffusion behavior and charge storage behavior. The EIS profiles shown in Fig. 6a comprise two parts, high-frequency semicircular and low-frequency inclined lines, representing charge transfer impedance (R_{ct}) and Warburg impedance (Z_w), respectively. As can be observed from the Nyquist plots, porous C@MoS_2 has the lowest charge transfer resistance.

We have provided the EIS at different current rates (Fig. S10†) of these two samples to better illustrate the performance differences, especially in relation to porosity. The EIS spectra reveal that porous C@MoS_2 exhibits lower ohmic resistances and charge transfer resistances (R_{ct}) than C@MoS_2, while its steeper low-frequency Warburg slopes indicate more efficient Na^+ ion transport, collectively confirming faster ion/charge transfer *via* macroporous carbon networks. The diffusion behavior of Na^+ can be expressed by the equation as follows:[58]

$$D = R^2T^2/2n^4F^4\sigma_w^2A^2C^2, \quad (1)$$

where D is the diffusion coefficient of Na^+, R is the gas constant, T is the absolute temperature, A is the surface area of the electrode, n is the number of electrons transferred per molecule in the electronic reaction, F is the Faraday constant, C is the concentration of Na^+, and σ_w is the slope of the line.

$$Z' = R + \sigma_w\omega^{-1/2} \quad (2)$$

As shown in Fig. 6b, the slopes (σ_w) of porous C@MoS_2 and C@MoS_2 are 315.9 and 547.9, respectively. The above results indicate that MoS_2 coated on a macroporous carbon framework exhibited better electrical conductivity and fast Na^+ reaction kinetics compared with MoS_2 on amorphous carbon, which is consistent with its excellent cycling and rate performance.

To further investigate the charge storage behavior of porous C@MoS_2, CV curves were obtained at different scan rates (0.4–1.0 mV s^{-1}). As shown in Fig. 6c, the peak current of the CV

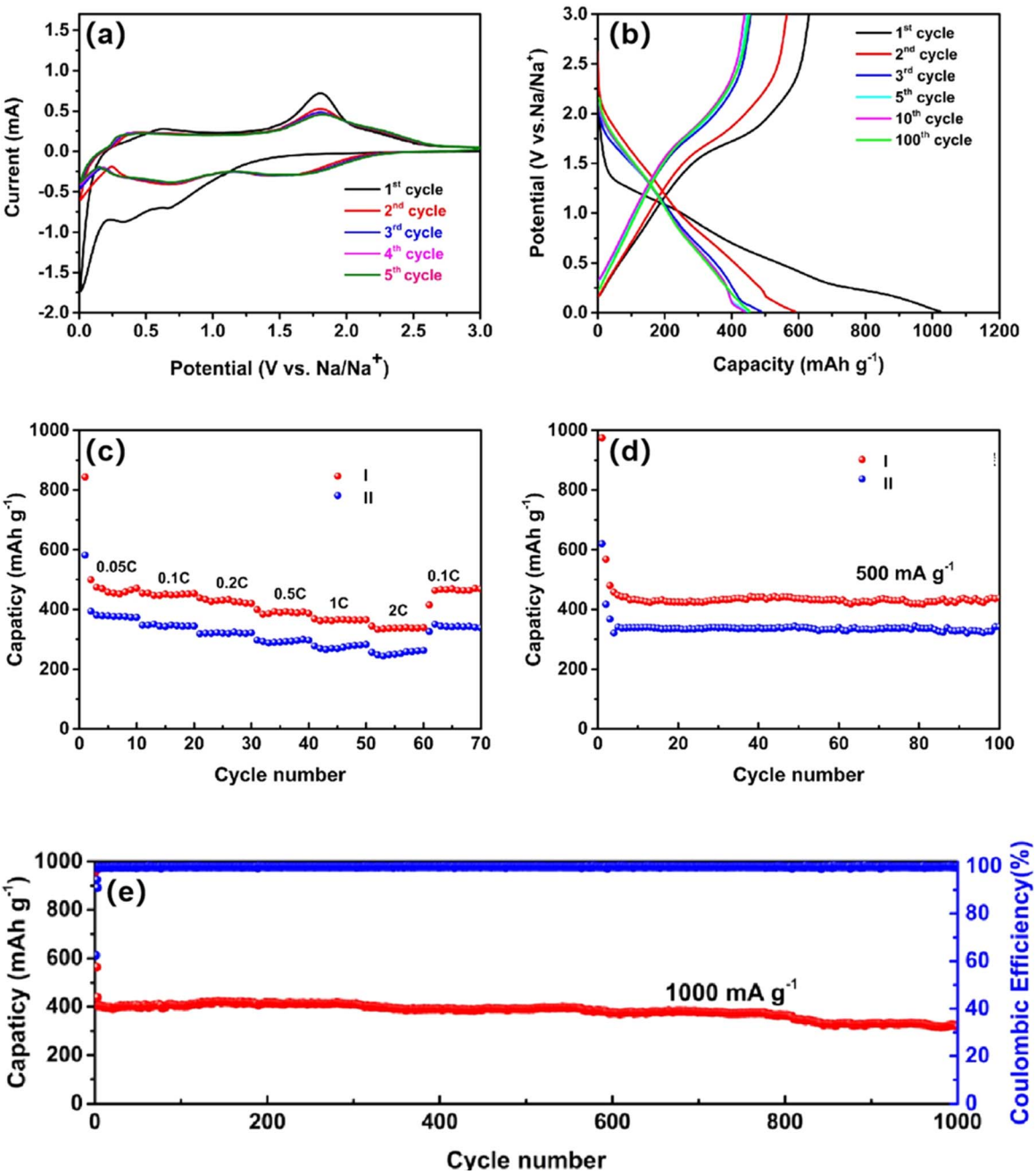

Fig. 5 Electrochemical performance of different samples. (a) CV curves of the porous C@MoS_2 for the first five cycles at a scan rate of 0.5 mV s^{-1}. (b) Galvanostatic discharge–charge curve of porous C@MoS_2 at 500 mA g^{-1}. (c) Cycling performance of the porous C@MoS_2 and C@MoS_2 at a current density of 500 mA g^{-1}. (d) Rate performances of the porous C@MoS_2 and C@MoS_2. We take 1000 mA h g^{-1} as a 1C rate according to the theoretical capacity of MoS_2 (670 mA h g^{-1}) and amorphous carbon (~350 mA h g^{-1}). (e) Long-term cycling property and coulombic efficiency of the porous C@MoS_2 at a current density of 1000 mA g^{-1}.

profiles increases as the scan rates increase, according to the following equations:

$$i = av^b \quad (3)$$

$$\log i = b \log v + \log a \quad (4)$$

where i is the measured current, a is the adjustable parameter, v is the scanning rate and b is the slope of the plot of log(i) *vs.* log(v). As illustrated in Fig. 6c and S12,† the b values of porous C@MoS_2 (0.874 and 0.812) are higher than those of C@MoS_2 (0.827 and 0.764). The b values are close to 1, indicating that both intercalation and capacitive capacity contribute to Na^+ storage, with the latter in the dominant position. The ratio of the capacitive contribution to the total capacity can be further determined using the following equation:[31]

$$i = k_1 v + k_2 v^{1/2} \quad (5)$$

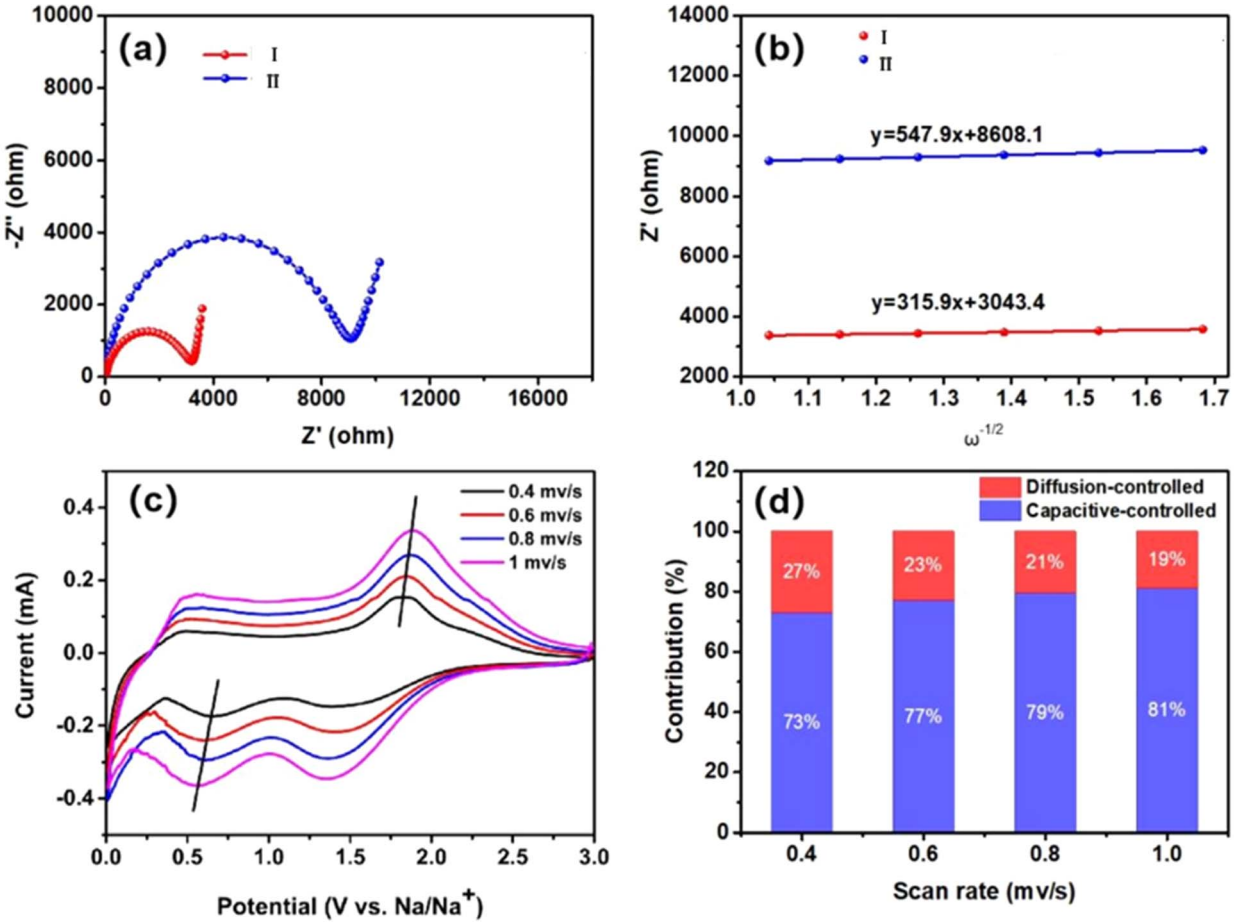

Fig. 6 (a) EIS Nyquist plots of porous C@MoS_2 (I) and C@MoS_2 before charging/discharging (II). (b) Relationship between Z' and $\omega^{-1/2}$ for porous C@MoS_2 (I) and C@MoS_2 (II). (c) CV curves of porous C@MoS_2 with different scan rates. (d) Contributions of the capacitive and diffusion-controlled storage at different scan rates of porous C@MoS_2.

where k_1v and $k_2v^{1/2}$ are related to capacitive-controlled and diffusion-controlled contributions, respectively. Fig. 6d shows that, for sample porous C@MoS_2, the capacitive storage contributes the major capacity as the sweep rate increases. The capacitive contributions are 73%, 77%, 79%, and 81% at sweep rates of 0.4, 0.6, 0.8, and 1 mV s^{-1}, respectively. The capacitive contributions for porous C@MoS_2 demonstrate a consistent increase from 73% to 81% as sweep rates increase from 0.4 to 1 mV s^{-1}, while C@MoS_2 shows a similar trend from 72% to 79%, indicating enhanced charge storage kinetics in the porous architecture.

4. Conclusions

Macroporous carbon–MoS_2 composite was prepared through a facile hydrothermal treatment method, with PS nanospheres as hard templates. In comparison with MoS_2 coated on amorphous carbon, the porous C@MoS_2 sample showed significantly improved electrochemical performance as anode in SIBs, providing a stable specific capacity of 438 mA h g^{-1} after 100 cycles at a current density of 500 mA g^{-1} and a capacity of 319.4 mA h g^{-1} after 1000 cycles at a high current density of 1000 mA g^{-1}. This super performance may originate from the increased specific surface area, enhanced electrical conductivity, and fast sodium ion transmission rate that is inherited from its unique macroporous structure of porous C@MoS_2. This study sheds light on the advantages of material structural design and can inspire the development of more advanced electrode materials for the application of high-performance sodium-ion batteries.

Data availability

The data supporting this article have been included as part of the ESI.†

Author contributions

Yan Yang contributed to conceptualization, funding acquisition, project administration, supervision and writing – review & editing of this work. Lei Wang contributed to methodology, data curation, validation and writing – original draft of this work. Cong Suo and Yining Liu assisted with data curation.

Conflicts of interest

There are no conflicts to declare.

Acknowledgements

This work was supported financially by the National Natural Science Foundation of China (No. 21905035), Liaoning Revitalization Talents Program (XLYC1907093).

References

1 V. Aravindan, J. Gnanaraj, Y. S. Lee and S. Madhavi, Insertion-type electrodes for nonaqueous Li-ion capacitors, *Chem. Rev.*, 2014, **114**, 11619–11635.
2 M. Wakihara, Recent developments in lithium ion batteries, *Mater. Sci. Eng., R*, 2001, **33**, 109–134.
3 M. Xu, Q. Yu, Z. Liu, J. Lv, S. Lian, B. Hu, L. Mai and L. Zhou, Tailoring porous carbon spheres for supercapacitors, *Nanoscale*, 2018, **10**, 21604–21616.
4 P. Phogat, S. Dey and M. Wan, Comprehensive review of Sodium-Ion Batteries: Principles, Materials, Performance, Challenges, and future Perspectives, *Mater. Sci. Eng., B*, 2025, **312**, 117870.
5 K. Chayambuka, G. Mulder, D. L. Danilov and P. H. L. Notten, From Li-Ion Batteries toward Na-Ion Chemistries: Challenges and Opportunities, *Adv. Energy Mater.*, 2020, **10**, 202001310.
6 Z.-H. Luo, D. Zhang, J.-X. Guo, F. Jiang, N.-L. Shen, Y.-F. Du, Z.-J. Jiang, T. Wang, X. Liu, X.-B. Cheng, *et al.*, Recent progress on the materials design towards thermally safe sodium-ion batteries, *J. Energy Chem.*, 2025, **102**, 555–575.
7 S. Awasthi, A review on the optimization of electrolytes to enhance lithium-ion batteries' safety and performance under abuse conditions, *J. Energy Storage*, 2024, **100**, 113439.
8 P. G. Balakrishnan, R. Ramesh and T. P. Kumar, Safety mechanisms in lithium-ion batteries, *J. Power Sources*, 2006, **155**, 401–414.
9 T. Qi, K. Xiong and X. Zhang, Research progress of carbon materials in the anodes of sodium-ion batteries, *J. Power Sources*, 2025, **626**, 235721.
10 M. H. Hossain, M. A. Chowdhury, N. Hossain, M. A. Islam, M. H. Mobarak, M. Hasan and J. Khan, Advances on synthesis and performance of Li-Ion anode batteries-a review, *Chem. Eng. J. Adv.*, 2024, **17**, 100588.
11 S. A. Riza, R.-g. Xu, Q. Liu, M. Hassan, Q. Yang, D.-b. Mu, L. Li, F. Wu and R.-j. Chen, A review of anode materials for sodium ion batteries, *New Carbon Mater.*, 2024, **39**, 743–769.
12 G. Li, H. Ma, Y. Tong, H. Wang, Y. Luo, E. H. Ang, S. Bohm, A. A. Ibrahim and A. Umar, Research progress on carbon-based anode materials for sodium-ion batteries, *J. Energy Storage*, 2025, **107**, 114977.
13 D. P. DiVincenzo and E. J. Mele, Cohesion and Structure in Stage-1 Graphite Intercalation Compounds, *Phys. Rev. B:Condens. Matter Mater. Phys.*, 1985, **32**, 2538–2541.
14 O. Lenchuk, P. Adelhelm and D. Mollenhauer, New Insights into the Origin of Unstable Sodium Graphite Intercalation Compounds, *Phys. Chem. Chem. Phys.*, 2019, **21**, 19378–19390.
15 Y. Wu and Y. Yu, 2D material as anode for sodium ion batteries: Recent progress and perspectives, *Energy Storage Mater.*, 2019, **16**, 323–343.
16 Y. Zhang, R. Zhang, Y. Guo, Y. Li and K. Li, A review on MoS_2 structure, preparation, energy storage applications and challenges, *J. Alloys Compd.*, 2024, **998**, 174916.
17 C. Liu, Y. Bai, Y. Zhao, H. Yao and H. Pang, MoS_2/graphene composites: fabrication and electrochemical energy storage, *Energy Storage Mater.*, 2020, **33**, 470–502.
18 B. Wang, Y. Xia, G. Wang, Y. Zhou and H. Wang, Core shell MoS_2/C nanospheres embedded in foam-like carbon sheets composite with an interconnected macroporous structure as stable and high-capacity anodes for sodium ion batteries, *Chem. Eng. J.*, 2017, **309**, 417–425.
19 Z.-T. Shi, W. Kang, J. Xu, Y.-W. Sun, M. Jiang, T.-W. Ng, H.-T. Xue, D. Y. W. Yu, W. Zhang and C.-S. Lee, Hierarchical nanotubes assembled from MoS_2-carbon monolayer sandwiched superstructure nanosheets for high-performance sodium ion batteries, *Nano Energy*, 2016, **22**, 27–37.
20 F. Ding, Y. Zhang, Y. Lei, Y. Yan, J. Huo, Y. Shen, X. Li and W. Kang, Application of MoS_2 in energy and its performance improvement strategy, *J. Energy Storage*, 2024, **104**, 114605.
21 X.-S. Yuan, S.-H. Zhou, S.-M. Wang, W. Wei, X. Li, X.-T. Wu and Q.-L. Zhu, Ordered macroporous superstructure of defective carbon adorned with tiny cobalt sulfide for selective electrocatalytic hydrogenation of cinnamaldehyde, *Appl. Catal., B*, 2025, **361**, 124642.
22 H. Wu, M. Yue, L. He, M. Zhang, Y. Huang, C. Sun, Y. Liu, J. Wang, R. Lv and R. Xing, Box-shaped necklace-like Fe_3O_4/MoS_2-CNFs composite nanofibers with confinement effect enhancing sodium storage performance, *Chem. Eng. J.*, 2025, **503**, 158230.
23 J. Shahbaz, M. R. Khawar, S. Jang, N. A. Shad, A. Ahmad, M. D. Albaqami, U. Zahid, K. Y. Rhee, Y. Javed and D. Choi, A hierarchical surface-coated 3D-nanoflower network of MoS_2 with abundant reaction sites for high-performance asymmetric supercapacitor, *J. Alloys Compd.*, 2025, **1010**, 177230.
24 C. Li, W. Lyu, R. Lin, H. Liu, Y. Wang, D. Chen, F. Wang and Y. Li, Three-dimensional ordered macroporous nitrogen-doped carbon for efficient adsorption of flavonoids from plant extraction, *Chem. Eng. J.*, 2025, **503**, 158609.
25 K. She, Y. Huang, W. Fan, M. Yu, J. Zhang and C. Chen, 3D flower-like hollow MXene@MoS_2 heterostructure for fast sodium storage, *J. Colloid Interface Sci.*, 2024, **656**, 270–279.
26 Y. Han, P. Zhang and X. Zhao, A review of 3D monolithic carbon-based materials with a high photothermal conversion efficiency used for solar water vapor generation, *New Carbon Mater.*, 2024, **39**, 240–253.
27 T. Han, Z. He, W. Kuang, J. Zhou and Y.-y. Li, 3D printing of porous hollow nanosphere MoS_2@NiS/rGO scaffolds empowering long-cycle sodium-ion batteries, *Nano Energy*, 2024, **128**, 109953.

28 J.-X. Li, L. Fan, Q. Hua, Q. Geng, Y. Zhang, X. Fan, L. Ma, C. Wang, W. Zhu, X. Feng, *et al.*, Ordered macroporous carbonous skeletons implanted with dual-phase Co/CoFe nanoparticles for boosting electrocatalytic performance, *Chem. Eng. J.*, 2023, **470**, 144399.

29 F. Zheng, Z. Wei, H. Xia, Y. Tu, X. Meng, K. Zhu, J. Zhao, Y. Zhu, J. Zhang, Y. Yang, *et al.*, 3D MoS_2 foam integrated with carbon paper as binder-free anode for high performance sodium-ion batteries, *J. Energy Chem.*, 2022, **65**, 26–33.

30 D. Alvira, D. Antorán, M. Vidal, V. Sebastian and J. J. Manyà, Vine Shoots-Derived Hard Carbons as Anodes for Sodium-Ion Batteries: Role of Annealing Temperature in Regulating Their Structure and Morphology, *Batteries Supercaps*, 2023, **6**, e202300233.

31 Z. Li, Z. Jian, X. Wang, I. A. Rodríguez-Pérez, C. Bommier and X. Ji, Hard Carbon Anodes of Sodium-Ion Batteries: Undervalued Rate Capability, *Chem. Commun.*, 2017, **53**, 2610–2613.

32 M. Li, N. Hong, J. Jiang and W. Fu, Coulombic interaction: the origin of hollow silica nanoparticles from charged polystyrene template, *Colloids Surf., A*, 2022, **648**, 129407.

33 D. Deepika and P. E. Jagadeeshbabu, Synthesis of silica hollow core shell nanoparticles by sacrificial nitrated polystyrene template approach for targeted drug delivery application, *Mater. Today: Proc.*, 2021, **45**, 740–744.

34 T. Yang, J. Liang, I. Sultana, M. M. Rahman, M. J. Monteiro, Y. Chen, Z. Shao, S. R. P. Silva and J. Liu, Formation of hollow MoS_2/carbon microspheres for high capacity and high rate reversible alkali-ion storage, *J. Mater. Chem. A*, 2018, **6**, 8280–8288.

35 X. Zhao, W. Cai, Y. Yang, X. Song, Z. Neale, H.-E. Wang, J. Sui and G. Cao, $MoSe_2$ nanosheets perpendicularly grown on graphene with Mo–C bonding for sodium-ion capacitors, *Nano Energy*, 2018, **47**, 224–234.

36 D. Gueon, J. T. Hwang, S. B. Yang, E. Cho, K. Sohn, D. K. Yang and J. H. Moon, Spherical Macroporous Carbon Nanotube Particles with Ultrahigh Sulfur Loading for Lithium-Sulfur Battery Cathodes, *ACS Nano*, 2018, **12**, 226–233.

37 J. Sun, S. Jiao, G. Lian, L. Jing, D. Cui, Q. Wang and C.-P. Wong, Hierarchical MoS_2/m-C@a-C@Ti_3C_2 nanohybrids as superior electrodes for enhanced sodium storage and hydrogen evolution reaction, *Chem. Eng. J.*, 2021, **421**, 129680.

38 Y. Tang, Z. Zhao, Y. Wang, Y. Dong, Y. Liu, X. Wang and J. Qiu, Ultrasmall MoS_2 Nanosheets Mosaiced into Nitrogen-Doped Hierarchical Porous Carbon Matrix for Enhanced Sodium Storage Performance, *Electrochim. Acta*, 2017, **225**, 369–377.

39 X. Yue, N. Huang, Z. Jiang, X. Tian, Z. Wang, X. Hao and Z.-J. Jiang, Nitrogen-rich graphene hollow microspheres as anode materials for sodium-ion batteries with super-high cycling and rate performance, *Carbon*, 2018, **130**, 574–583.

40 H. Yu, Z. Wang, J. Ni and L. Li, Freestanding nanosheets of 1T-2H hybrid MoS_2 as electrodes for efficient sodium storage, *J. Mater. Sci. Technol.*, 2021, **67**, 237–242.

41 Y. Xiao, Q. Le, Y. Kong, W. Lv, D. Su, X. Rui, S. Yu, A. Zhang, J. Zhao, Q. Yang, *et al.*, Ultrafast and ultrastable Na-ion storage in interface engineered MoS_2/MXene nanohybrids with nanoconfinement for high-performance sodium-ion capacitors, *Chem. Eng. J.*, 2025, **505**, 159268.

42 Y. Wang, Y. Yang, D. Zhang, Y. Wang, X. Luo, X. Liu, J. K. Kim and Y. Luo, Inter-overlapped MoS_2/C composites with large-interlayer-spacing for high-performance sodium-ion batteries, *Nanoscale Horiz.*, 2020, **5**, 1127–1135.

43 K. Chang, W. Chen, L. Ma, H. Li, H. Li, F. Huang, Z. Xu, Q. Zhang and J.-Y. Lee, Graphene-like MoS_2/amorphous carbon composites with high capacity and excellent stability as anode materials for lithium ion batteries, *J. Mater. Chem.*, 2011, **21**, 6251–6257.

44 X. Y. Yu, H. Hu, Y. W. Wang, H. Y. Chen and X. W. Lou, Ultrathin MoS_2 Nanosheets Supported on N-doped Carbon Nanoboxes with Enhanced Lithium Storage and Electrocatalytic Properties, *Angew. Chem., Int. Ed.*, 2015, **54**, 7395–7398.

45 W. Sun, K. Guo, J. Fan, Y. Min and Q. Xu, Confined Selenium in N-Doped Mesoporous Carbon Nanospheres for Sodium-Ion Batteries, *ACS Appl. Mater. Interfaces*, 2021, **13**, 16558–16566.

46 J. Wang, J. Liu, H. Yang, D. Chao, J. Yan, S. V. Savilov, J. Lin and Z. X. Shen, MoS_2 nanosheets decorated Ni_3S_2@MoS_2 coaxial nanofibers: Constructing an ideal heterostructure for enhanced Na-ion storage, *Nano Energy*, 2016, **20**, 1–10.

47 Y.-Y. Hu, Y.-L. Bai, X.-Y. Wu, X. Wei, K.-X. Wang and J.-S. Chen, MoS_2 nanoflakes integrated in a 3D carbon framework for high-performance sodium-ion batteries, *J. Alloys Compd.*, 2019, **797**, 1126–1132.

48 Z. Yuan, L. Wang, D. Li, J. Cao and W. Han, Carbon-Reinforced Nb_2CT_x MXene/MoS_2 Nanosheets as a Superior Rate and High-Capacity Anode for Sodium-Ion Batteries, *ACS Nano*, 2021, **15**, 7439–7450.

49 Y. Fang, Y. Y. Lv, F. Gong, A. A. Elzatahry, G. F. Zheng and D. Y. Zhao, Synthesis of 2D-Mesoporous-Carbon/MoS_2 Heterostructures with Well-Defined Interfaces for High-Performance Lithium-Ion Batteries, *Adv. Mater.*, 2016, **28**, 201602210.

50 X. Xie, T. Makaryan, M. Zhao, K. L. Van Aken, Y. Gogotsi and G. Wang, MoS_2 Nanosheets Vertically Aligned on Carbon Paper: A Freestanding Electrode for Highly Reversible Sodium-Ion Batteries, *Adv. Energy Mater.*, 2016, **6**, 201502161.

51 C. Zhu, X. Mu, P. A. van Aken, J. Maier and Y. Yu, Fast Li Storage in MoS_2-Graphene-Carbon Nanotube Nanocomposites: Advantageous Functional Integration of 0D, 1D, and 2D Nanostructures, *Adv. Energy Mater.*, 2015, **5**, 201401170.

52 J. W. Zhou, J. Qin, X. Zhang, C. S. Shi, E. Z. Liu, J. J. Li, N. Q. Zhao and C. N. He, 2D Space-Confined Synthesis of Few-Layer MoS_2 Anchored on Carbon Nanosheet for Lithium-Ion Battery Anode, *ACS Nano*, 2015, **9**, 3837–3848.

53 X. Zhang, R. F. Zhao, Q. H. Wu, W. L. Li, C. Shen, L. B. Ni, H. Yan, G. W. Diao and M. Chen, Petal-like MoS_2 Nanosheets Space-Confined in Hollow Mesoporous Carbon

Spheres for Enhanced Lithium Storage Performance, *ACS Nano*, 2017, **11**, 8429–8436.

54 N. Nieto, J. Porte, D. Saurel, L. Djuandhi, N. Sharma, A. Lopez-Urionabarrenechea, V. Palomares and T. Rojo, Use of Hydrothermal Carbonization to Improve the Performance of Biowaste-Derived Hard Carbons in Sodium-Ion Batteries, *ChemSusChem*, 2023, **16**, e202301053.

55 Q. Zhang, Z. Wang, X. Li, H. Guo, J. Wang and G. Yan, Unraveling the role of LiODFB salt as a SEI-forming additive for sodium-ion battery, *Ionics*, 2020, **27**, 683–691.

56 Y. Li, H. Mao, C. Zheng, J. Wang, Z. Che and M. Wei, Compositing Reduced Graphene Oxide with Interlayer Spacing Enlarged MoS_2 for Performance Enhanced Sodium-Ion Batteries, *J. Phys. Chem. Solids*, 2020, **136**, 109163.

57 S. H. Choi, Y. N. Ko, J.-K. Lee and Y. C. Kang, 3D MoS_2–Graphene Microspheres Consisting of Multiple Nanospheres with Superior Sodium Ion Storage Properties, *Adv. Funct. Mater.*, 2015, **25**, 1780–1788.

58 X. Dong, Z. Xing, G. Zheng, X. Gao, H. Hong, Z. Ju and Q. Zhuang, MoS_2/N-doped graphene aerogels composite anode for high performance sodium/potassium ion batteries, *Electrochim. Acta*, 2020, **339**, 135932.